Distributed Intelligence for Online Situational Awareness in Power Grids

Shiyuan Wang, *Member, IEEE*, Li Li, *Member, IEEE*, and Payman Dehghanian, *Senior Member, IEEE*

***Abstract*—This paper presents a suite of analytics that are proposed to be embedded in next-generation smart sensors in electric power grids. The proposed analytics take the electrical signals as the input and unlock the full potential in signal processing and machine learning for real-time event detection and classification. Meanwhile, a robust synchrophasor estimation mechanism is housed within the proposed sensor technology that will be triggered following a detected event and guides on the adaptive selection of the best-fit (most accurate) synchrophasor estimation algorithms at all times. Embedding such analytics within the sensor and closer to where the waveforms are captured, the proposed distributed intelligence solution technology mitigates the potential risks to communication failures and latencies as well as malicious cyber threats. Our experiments demonstrate that the introduced scheme achieves improved quality of measurements with a promising event detection and classification accuracy, collectively resulting in enhanced online situational awareness in modern power grids.**

***Index Terms*—Feature extraction, event detection, machine learning, situational awareness, signal processing, smart sensor, synchrophasor estimation, waveform classification.**

I. Introduction

A. Problem Statement and Existing Challenges

WIDESPREAD deployment of Phasor Measurement Units (PMUs) has dramatically changed the traditional sensing and measurement paradigms in power grids into a new setting with high-resolution measurements [1]–[3]. Synchrophasors captured from distributed PMUs across the power grid have transformed many control center analytics in power systems. PMUs are typically classified into two types, i.e., M-Class PMUs providing measurements satisfying high-accuracy standard requirements or P-Class PMUs fulfilling the high-speed low-latency measurement requirements. Relevant synchrophasor estimation algorithms within the PMU sensors are serving real-time measurements for many end-use applications, e.g., online monitoring, protection and control, state estimation, dynamic stability assessment, power system model validation, and post-event analyses [4]–[6].

The existing monitoring and control paradigms in power systems are primarily based on centralized architectures. That is, the sensing landscape consists of locally distributed PMUs, the measurements from which are collected in distant control centers for monitoring and control decision making. This current practice relies heavily on reliable and secure communication gateways: if the communication channels are lost (due to failures, natural disasters, or man-made cyber-attacks) or have delays (due to communication network congestion, poor channel quality, etc.), the accuracy and trustworthiness of the control center analytics using such measurements would be compromised or attributed a latency. Eliminating such potential risks, system monitoring and control paradigms should enable fusing the online measurements in a distributed manner; that is building in distributed intelligence and translating the data into valuable information closer to where the data is generated (i.e., in electric substations).

Additionally, the trustworthiness of the control center functions heavily relies on accurate synchrophasor measurements from PMU sensors; these measurements are achieved from synchrophasor estimation algorithms (SEAs) embedded within the PMUs which are primarily driven by mathematical approximations, such as, Short Time Fourier Transform, Phase-Locked Loops, Kalman Filtering, Newton Approximations, and many other variations [7]–[12]. IEEE standard C37.118.1-2011 [13] has established the definition of PMU outputs–i.e., magnitude, phase angle, frequency, and rate of change of frequency (ROCOF)—and their corresponding measurement compliance. In most cases, and with no consideration to the end-use applications utilizing the measurements, marketplace PMUs are typically furnished with "only one" SEA tool, each unleashing distinctive advantages and limitations, and are solely accurate for one or a few certain applications using PMU measurements [14], [15]. This is because the waveforms fed into PMUs have typically variant behaviors (e.g., during faults, unbalanced loads, voltage surge or sag, harmonics, etc) [16], [17]. Also, different applications using synchrophasor measurements may enforce

Manuscript received July 16, 2020; revised March 18, 2021 and August 5, 2021; accepted November 7, 2021. Date of publication November 18, 2021; date of current version June 20, 2022. This work was supported in part by the US Department of Energy (DOE) Office of Electricity's Electricity Industry Technology and Practices Innovation Challenge (EITPIC) and the National Science Foundation (NSF) under Grant ICER-2022505. Paper no. TPWRS-01201-2020. *(Corresponding author: Payman Dehghanian.)*

Shiyuan Wang was with the Department of Electrical and Computer Engineering, The George Washington University, Washington DC 20052 USA and is now with the Quanta Technology, LLC., Raleigh, NC 27607 USA (e-mail: shiyuan1225@gwu.edu).

Li Li was with the Department of Electrical and Computer Engineering, The George Washington University, Washington DC 20052 USA, and is now with the Advanced Micro Devices (AMD), Austin, TX 78735 USA (e-mail: lili1986@gwu.edu).

Payman Dehghanian is with the Department of Electrical and Computer Engineering, The George Washington University, Washington DC 20052 USA (e-mail: payman@gwu.edu).

Color versions of one or more figures in this article are available at https://doi.org/10.1109/TPWRS.2021.3128951.

Digital Object Identifier 10.1109/TPWRS.2021.3128951

different response time and accuracy requirements. Some researchers proposed a single PMU scheme furnished with only one sophisticated SEA, aiming to respond to all kinds of predictable or random conditions in the grid [18], [19]. Results from both laboratory tests and field observations have revealed how inefficient the PMU measurements could be, if this "one-size-fits-all" SEA is applied to capture both static and dynamic features and peculiarities in power systems, when facing different operating states and driving phenomena. In particular, lab tests in [20] have shown that some PMU outputs failed to be compliant with the standard requirements under some operating conditions such as off-nominal frequencies, modulations, etc. To overcome this, adaptive phasor estimation approaches such as adaptive filtering [21], adaptive window with localization of waveform discontinuities [22], and magnitude/frequency dynamic identification [23], [24], etc., have been proposed and are available in the literature. However, these adaptive control signals in conventional adaptive phasor measurement methodologies can only indicate *the existence* of dynamics in the waveforms, but cannot provide sufficient information on the ongoing event or the cause of the dynamics, thereby resulting in limited situational awareness for the system operators. Furthermore, the phasor measurements are still needed to be transmitted to distant control centers for monitoring and control decisions, thereby in need of fast and reliable communication channels yet vulnerable to failures, delays, etc.

B. Literature Review

Event detection and classification are indeed one main focus of what is called "online situational awareness" in power grids. The term "situational awareness" in the context of electric power grid operation is defined as "understanding the current environment and being able to accurately anticipate future problems to enable effective actions" [25]. Situational awareness is a key factor in preserving power system security, as it enables effective and timely decision-making and adaptive control in response to an unfolding incident [26]. Due to the increasing size and operational complexity of modern power systems, transmission system operators often have difficulties forming a complete and accurate picture of the state of the system, limiting the level of situational awareness that is needed to make the right decisions and respond effectively to an incident. Inadequate situational awareness has indeed been identified as one contributing factor in several recent large electrical disturbances worldwide [27], [28]. In November 2006, an inadequate situational awareness initiated a cascade of events and resulted in the separation of the European Grid into three regions with different frequencies [29]. According to [26], situational awareness encompasses three separate levels: (1) achieving information on key elements of the power grid; (2) Understanding what the perceived data means in relation to the operators' objectives; and (3) Projecting the future behavior of the system components based on their current state and on the perceived information.

The existing event detection and classification approaches in the literature are mainly based on centralized architectures, irrespective of how the phasor measurements are achieved. A PMU measurement-based event detection mechanism using dynamic programming-based swinging door trending algorithm is proposed in [30]. This approach requires a huge amount of streaming PMU data, and a time synchronization, uncongested communication, and identical PMU communication delays. Researchers in [31] proposed a centralized event detection algorithm via computation of the spectral kurtosis on the sum of the intrinsic mode functions. This approach relies on the continuous data streams collected via PMUs installed at different locations across the power grid. Therefore, it is vulnerable to communication losses or delays. Principal component analysis (PCA) is one of the most popular multivariate statistical techniques for dimensionality reduction and has been widely used in various fields [32]. A PCA-based method for detection and classification of multiple events using frequency data from multiple PMUs is proposed in [33], which can detect loss of generation and/or loads. Similarly, authors in [34] proposed a partitioned PCA-based algorithm to reduce the computational burden in analyzing volumes of PMU measurements. However, an event detection and classification rule is still required for effective decision making in real-time. An abnormal event detection application using a micro-phasor measurement unit (μPMU) in the distribution system is proposed in [35]. In response to the challenges in processing multiple streams of high-resolution data, a pooling-picking scheme is first applied, a kernel PCA (kPCA) is then adopted to build the statistical models, and a partially-hidden structured support vector machine (pSVM) is finally used to classify and distinguish a variety of events. In summary, the aforementioned approaches rely on *centralized* analytics employing measurements from *multiple* PMUs across the power grid through *seamless communication* channels. With the massively-growing adoption of computing engines/nodes in smart grids, a variety of distributed real-time analysis and control frameworks are proposed and implemented [36]–[40]. One notable advantage of the distributed intelligent control compared to the centralized mechanisms is the significant reduction in data communication and complexity, resulting in better utilization of the communication bandwidth.

C. Contributions

To the best of our knowledge, there is no scheme available in the literature to address the detection and classification of multiple events locally, particularly by relaying only on the original waveforms captured on a single point of measurement. Tackling the aforementioned challenges and for effectively addressing fast and slow-transient disruptions in power grids, this paper introduces the *next-generation smart sensors* in power grids. Embedded with advanced signal processing and machine learning algorithms, the proposed smart sensor solution with built-in intelligence enables a paradigm shift from *sensing-only* to *sensing-and-actuating* mechanisms that can achieve decentralized online event detection, classification, and high-fidelity measurements in power grids. In an end-to-end modular platform, the proposed smart sensor will trigger fast and robust control actions against the detected disruptions. The main contributions of this paper are as follows:

- A pseudo-continuous quadrature wavelet transform (PCQ-WT) is proposed that processes (voltage and current) waveforms and effectively performs an online pattern recognition and feature extraction.
- Built on the PCQ-WT-extracted features, a machine learning mechanism, i.e., the convolutional neural network (CNN), is developed to detect and classify different event scalograms in real-time.
- Founded on the Quadrature Delayed Signal Cancellation (QDSC) and Gaussian Weighted Taylor series (GWT) principles, two fast and accurate SEAs, which respectively meet the IEEE standards for P-Class and M-Class measurements, are developed.
- An efficient SEA selection scheme is proposed and housed within the smart sensor that adaptively selects the most promising SEA algorithm which best suites the detected event and ensures high-fidelity measurements.

The rest of the paper is structured as follows: A big-picture overview of the proposed sensor technology is introduced in Section II. Section III presents a brief background on the wavelet transforms and CNN. The proposed framework is analytically elaborated in Section IV. The performance of each analytical module within the proposed framework is numerically analyzed under a variety of events in Section V. And finally come the concluding remarks in Section VI.

II. The Big Picture of the Proposed Smart Sensor

A. Problem Statement

It has been demonstrated in the existing literature that a pre-installed SEA inside the PMU sensors needs to be chosen carefully or tuned at times to meet the performance requirements of the end-use applications employing the measurements [18], [19]. While exposed to different operating conditions in the power grid, a particular SEA may best work for one certain type of event. Moreover, an SEA can be tuned with distinct parameters, making it extremely difficult to achieve the desired accuracy at all times. Therefore, the measurement performance of the PMU would be improved if an event type could be detected in real-time and, accordingly, a proper SEA is selected in an automated manner.

Driven by the variant system operating conditions, waveforms in the power grid reveal specific patterns with unique features and peculiarities. For instance, waveform magnitudes and angles can experience step changes during faults; measurement noise can vary; the occurrence of voltage surge or sag, unbalanced load conditions, harmonics, and frequency drift, etc., can also be commonly observed in the waveform. The event classification problem in power grids could be then decomposed into two steps. First, the signatures and dominant patterns from the electrical waveforms, which carry valuable information on the underlying events, are extracted. Second, a classifier is employed for event detection and classification based on the extracted features.

B. Overview of the Proposed Embedded Analytics

Fig. 1 illustrates the algorithmic process proposed to be embedded within the smart sensors, characterized through the following four stages: (i) signal acquisition, (ii) feature extraction, (iii) event detection; and (iv) SEA selection.

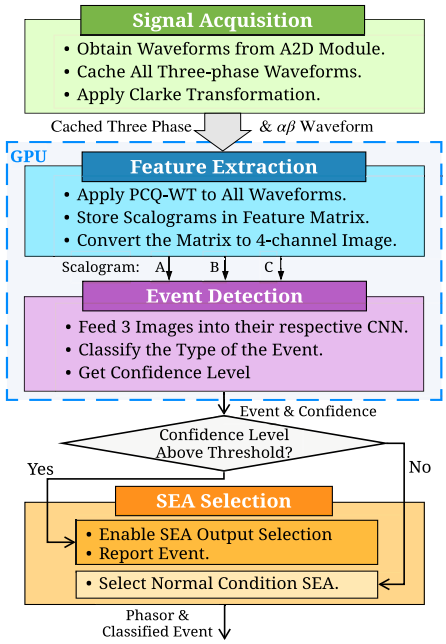

Fig. 1. Big picture of the algorithmic process within a smart sensor.

The proposed technology shares exact same input signals (voltage and current) as the existing PMUs in power grids, with no additional device nor investment for data acquisition. *First*, the sampled waveforms captured by the Analog to Digital (A2D) converter within the proposed sensor are loaded into the buffer. *Second*, the original waveforms are individually processed and features (scalograms) are extracted using the proposed PCQ-WT signal processing algorithm. To accelerate the consequent event classification, the scalograms are converted into images. The event classification in the *Third* step is, therefore, recast as an image classification process, where the scalograms are fed into CNN modules running in the Graphical Processing Unit (GPU) for event detection and classification. Since the processing time must be sufficiently short for online applications, a simple CNN architecture is proposed that also meets a designated accuracy requirement under a wide range of fast- and slow-dynamic events in power grids. The machine learning mechanism detects and classifies the event attributes with a confidence level. Under certain circumstances, the patterns/features in the scalograms could be extremely similar for different types of events, and the predicted event (with the highest confidence level) could interchange between several types in a short transient period of time. Hence, a threshold criterion for the output confidences is established to make a solid decision on the event detection and classification. Following the detected event (with the confidence level above a threshold), an adaptive SEA selection mechanism is devised in the *fourth* step that will adopt the most promising SEA outputs among a suite of embedded SEAs (high-speed and high-accuracy algorithms) for online measurements. If the confidence level is reported lower than the designated threshold, the system is concluded to be in its normal operating condition,

and the default SEA output will be used for accurate measurements. The hardware architecture of the proposed smart sensor technology is illustrated in Appendix I in [41].

III. Background

A. Cwt and Pseudo-Cwt

As the combinations of harmonic components contain valuable information; waveform time-frequency analytics can be utilized to evaluate the signal signatures and dominant features, i.e., amplitude, frequency, and phase angle. Features that might be undetected using one fixed resolution could be easily identified by using other resolutions. In this regard, wavelet transforms (WT) provide multi-resolution analysis and rich frequency information about the original signal. Meanwhile, the event detection module would benefit from the waveform features rather than detailed harmonic frequency measurement. Therefore, in this paper, wavelet analysis is selected as the main mathematical tool for online feature extraction.

The wavelet transform can be seen as the computation of the similarities between the signal of interest $x(t)$ and the selected wavelet, which can be written as follows:

$$X(\omega|a,b)=\frac{1}{\sqrt{|a|}}\int_{-\infty}^{\infty}x(t)\Psi^{*}\left(\frac{t-b}{a}\right)dt, \tag{1}$$

where a and b are the scaling factor and time shift, $\Psi(t)$ is the selected wavelet (called mother wavelet when $a=1$ and $b=0$), and "*" stands for complex conjugate operation. With different values of a and b selected, $\Psi(\frac{t-b}{a})$ becomes the "daughter wavelets" of $\Psi(t)$ [42], [43]. With a proper selection of *continuous* scaling factor intervals along with the time shifts, a CWT is achieved.

In the smart sensor solution, the input waveforms are first sampled; hence, the actual behavior of the conventional CWT within the processor is discrete WT with a set of discrete scaling factors a^i, wherein, i is an integer. To obtain more informative waveform features in the scalogram, a set of linearly-increasing real numbers are assigned to i in the proposed *Pseudo*-CWT. Similar to the discrete WT, the PCWT with one discrete scaling factor can be written as follows:

$$X[\omega|a_k,b_k]=\frac{1}{\sqrt{|a_k|}}\sum_{n=0}^{W-1}x[n]\Psi^{*}\left[\frac{nT_s-b_k}{a_k}\right], \tag{2}$$

where T_s is the sampling time, and W is the number of data samples in the buffer. Once a set of scaling factors with length K is selected, the wavelet bank $\boldsymbol{\Psi}$ and its extracted features (scalograms) at time n can be expressed as follows:

$$\boldsymbol{\Psi}^{K\times W}=\left[\Psi[\tfrac{nT_s-b_1}{a_1}],\ldots,\Psi[\tfrac{nT_s-b_k}{a_k}],\ldots,\Psi[\tfrac{nT_s-b_K}{a_K}]\right]^{\mathcal{T}}, \tag{3}$$

$$\mathbf{X}_{\underline{\omega}}[n]=\left[X_{\omega 1}(a_1,b_1),\ldots,X_{\omega k}(a_k,b_k),\ldots,X_{\omega K}(a_K,b_K)\right]^{\mathcal{T}}, \tag{4}$$

where, $\mathcal{T}$ is the conventional transpose. Since a window (buffer) of data samples is required during the feature extraction process, a latency effect exists; therefore, the selection of a proper window size should balance the latency and the sufficient length of the waveform.

B. Convolutional Neural Networks (CNNs)

In the event detection stage, the obtained scalograms are converted into 2-D images, and the classification of scalograms turns into a supervised image classification process. The conventional approach for image classification requires developing the feature extractor manually. This approach relies highly on the performance of the developed feature extractor. In contrast, Convolutional Neural Networks (CNNs) offer the capability of learning the features/representations automatically and have been proven very effective in processing image-related tasks [44]–[46]. Since PCQ-WT is fundamentally a linear transformation, the data entries in a scalogram are temporally-correlated. With the two-dimensional output of the PCQ-WT, CNN is a natural choice to process such kind of data [47]. It can exploit the correlation in the neighborhood in two-dimensional data (in its early layers) and abstract class information underlying the data distribution in the deeper layers [48], even if the class boundaries are complex and nonlinear in very high dimensional space, like the scalograms. In general, the execution of convolutional layers is achieved through the following set of cross-correlation assessments:

$$\boldsymbol{s}^{p}(m,n)=\sum_{u}\sum_{v}\sum_{w}\boldsymbol{I}^{u}(m+v,n+w)\boldsymbol{K}^{p}(v,w), \tag{5}$$

where $\boldsymbol{s}^{p}(m,n)$ stands for the convolutional layer's output at position (m,n) and p-th channel; the u-th convolutional kernel is marked as $\boldsymbol{K}^{u}$; and $\boldsymbol{I}^{u}$ denotes the image/data volume in the u-th channel. A complex convolutional layer is comprised of a set of simple layers [49], as expressed in the following:

$$\boldsymbol{I}_{l}=pool\left(\sigma(\boldsymbol{s})\right), \tag{6}$$

here $\boldsymbol{I}_{l}$ stands for the l-th layer's output volume; $\sigma(\cdot)$ stands for the nonlinear operation of the active function; and $pool(\cdot)$ is a pooling (down-sample) operation in the pooling layer. The abstraction ability of the network generally increases with the number of stacked convolutional layers [48].

IV. Proposed Analytics Within Smart Sensors

A. The Proposed PCQ-WT for Online Feature Extraction

To identify an event in each phase, the corresponding features need to be observed over time. As the positive-sequence frequency and phase angles are of interest in $x_{ph}(t)$ for synchrophasor measurements, a quadrature PCWT is proposed to extract the waveform features and signal signatures. To achieve a computationally-attractive solution with high-fidelity feature extraction performance, a complex Gabor wavelet is adopted in this paper, which is expressed as follows

$$\Psi(t)=\underbrace{exp\left(j\omega_c(t-b)\right)}_{\substack{\text{Periodic}\\ \text{Component}}}\cdot\underbrace{exp\left(-\frac{(t-b)^2}{\alpha_0^2}\right)}_{\substack{\text{Gaussian}\\ \text{Envelope}}}, \tag{7}$$

where, w_c is the central frequency. The Fourier transform of this Gabor wavelet is

$$\mathbf{F}_{\Psi}(\omega) = \alpha_0\sqrt{\pi}\cdot exp(-j\omega b)\cdot exp\left(-\frac{\alpha_0^2}{4}(\omega-\omega_c)^2\right). \quad (8)$$

One can see that the central frequency determines the pseudo frequency coverage in the waveform feature extraction process. According to (8), this Gabor wavelet possesses a predictable narrow bandwidth through properly selecting α_0, while the time shift b will not affect the magnitude of (8), i.e., the intensity of the extracted feature. Hence, to simplify the derivation, let $b=0$; then the CWT using the Gabor wavelet for a unit-length phasor with frequency $\omega_0 > 0$ turns into

$$\begin{aligned} X^{+}(\omega_0|a,b=0) &= \int_{-\infty}^{\infty} x(t)\Psi^{*}(\frac{t}{a})\mathrm{d}t \\ &= \int_{-\infty}^{\infty} exp\left(j\left(\omega_o-\frac{\omega_c}{a}\right)t-\frac{t^2}{a^2\alpha_0^2}\right)\mathrm{d}t. \end{aligned} \quad (9)$$

According to the Hubbard–Stratonovich transformation [50],

$$exp\left(-\frac{\alpha}{2}x^2\right) = \sqrt{\frac{1}{2\pi\alpha}}\int_{-\infty}^{\infty} exp\left(-\frac{y^2}{2\alpha}-jxy\right)\mathrm{d}y, \quad (10)$$

the Gabor wavelet transform in (9) turns into

$$X^{+}(\omega_0|a,b=0) = a\alpha_0\sqrt{\pi}exp\left(-\frac{\alpha_0^2}{4}(a\omega_0-\omega_c)^2\right). \quad (11)$$

It can be seen that when $\omega_0=\omega_c/a$, $X^{+}(\omega_0|a,b=0)$ reaches its maximum value; it indicates that the dominant feature of the selected frequency is extracted. Let

$$\alpha_0 = \omega_c/(\gamma a), \quad (12)$$

where, γ is a constant. Accordingly, and based on (7), the length of the Gaussian window in the Gabor wavelet also adapts different frequencies. While applied to the sinusoidal waveform, the feature corresponding to a phasor with negative frequency $(-\omega_0)$ is always suppressed, because the Gabor WT of the negative frequency in (13) decreases as ω_0 increases.

$$X^{-}(\text{-}\omega_0|a,b=0) = a\alpha_0\sqrt{\pi}exp\left(-\frac{\alpha_0^2}{4}(a\omega_0+\omega_c)^2\right). \quad (13)$$

The proposed Gabor WT that is used in a smart sensor can be expressed as

$$\Psi[n|a_k,b_k] = exp\left(j\frac{\omega_c T_s(n-b_k)}{a_k}\right)exp\left(-\frac{T_s^2(n-b_k)^2}{a_k^2\alpha_0^2}\right). \quad (14)$$

Applying different discrete scaling factors a_k and time shift b_k, the proposed PCQ-WT used in a smart sensor is obtained as,

$$\begin{aligned} X(\omega_k|a_k,b_k=0) &= \sum_{n=0}^{W-1} x[n]\Psi^{*}\left[-\frac{T_s n}{a_k}\right] \\ &= \sum_{n=0}^{W-1} x[n]exp\left(-j\frac{\omega_c}{a_k}T_s n-\frac{T_s^2 n^2}{a_k^2\alpha_0^2}\right). \end{aligned} \quad (15)$$

Then $\mathbf{X}_{\underline{\omega}}$ consisted of a set of PCQ-WTs is achieved, i.e., scalograms are generated which reveal the waveform signatures in frequencies of interest.

B. The Proposed CNN for Event Detection & Classification

As discussed earlier, the event detection problem can be recast to a supervised classification process based on the scalograms. However, classification of the high-dimensional 2-D scalograms is challenging due to the high dimensionality. Specifically, every frame of the obtained scalogram has hundreds by hundreds $(scales \times time)$ pixels. Therefore, the PCQ-WT scalograms are converted to 2-D images, and a compact CNN to classify scalograms which convey valuable information about the events in power systems is proposed. Since the classification of the generated scalogram does not have a very high abstraction level, the proposed CNN has a simple architecture that provides accurate event detection results yet achieving a fast processing speed. This framework can be either a standalone tool for event detection and classification or can be functionally embedded within PMUs assisting the phasor processor in selecting proper SEA outputs in real-time.

C. The Proposed Adaptive Phasor Estimation

The event detection and classification module introduced in Section IV-B provides real-time information on the grid operating conditions. The one-size-fits-all algorithm within the existing PMUs may neither be sufficient nor accurate in effectively dealing with all types of signals corresponding to different events and operating conditions in power grids. Multiple solutions can be thought in response to this challenge: (i) one very costly solution would be to install several different sensors (each with one different SEA) in each substation for different end-use applications that use the measurements; (ii) the other approach can be to design one very accurate SEA that can work very effectively under all system operating conditions meeting all measurement accuracy and speed requirements, which is extremely hard to achieve considering the hardware limitations as well as the ever-existing trade-off between the speed-accuracy performance requirements for different applications; (iii) one promising and viable approach in line with today's and tomorrow's infrastructure and computing technologies—which this paper focuses on—is to host a suite of SEAs that work in parallel within the sensor and are selectively and adaptively activated in an automated manner depending on the unfolded system operating condition.

The detailed architecture of the proposed SEA selection module is shown in Fig. 2. For every detected event and identified operating condition, the best-fit measurements—phasor, frequency and ROCOF—are selected in real-time; therefore, the output selector should be equipped with an optimized strategy that dynamically switches between one or multiple SEAs. Among SEAs within the smart sensor, two novel SEAs are proposed, one P-Class with promising estimation speed and one M-Class with high-accuracy measurements.

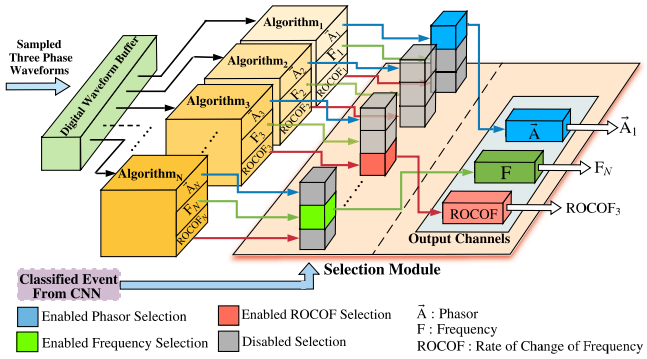

Fig. 2. Architecture diagram of the developed SEA selection module.

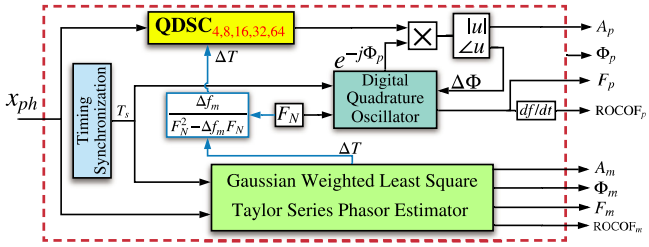

Fig. 3. The proposed P-Class and M-Class SEAs within a smart sensor.

D. The Proposed P-Class and M-Class SEAs

The overall architecture for the proposed P-Class and M-Class SEAs within a smart sensor is presented in Fig. 3. The sampled waveform is sent into the Quadrature Delay Signal Cancellation (QDSC) module to estimate the P-Class phasor magnitude (A_p). A functionally-programmed digital quadrature oscillator is used to assess the P-Class phase angle (Φ_p) and frequency (F_p) through eliminating the phase difference ($\Delta\Phi$) between the fundamental waveform and the quadrature oscillator. At last, the ROCOF$_p$ is estimated through the derivative of the measured frequency F_p. The M-Class phasor magnitude (A_m), phase angle (Φ_m), frequency (F_m), and ROCOF$_m$ are estimated from the Gaussian-Weighted Least Square Taylor Series SEA. Here, the proposed M-Class SEA is abbreviated as "GWT-M". Meanwhile, the GWT-M provides the deviation of the waveform nominal period (ΔT) to the QDSC module. This, in turn, makes the proposed P-Class measurement adaptive to designated operating conditions. In our proposed framework, the timing synchronization is employed to drive the digital oscillator and to ensure an accurate measurement. The nominal fundamental frequency (F_N) and the period (T_N) is determined by the system frequency, i.e., 50 Hz or 60 Hz.

1) The Proposed P-Class SEA, Dynamic QDSC Filter Algorithm: The structure of the proposed QDSC algorithm is presented in Fig. 4. The discretely-sampled waveform x_{in} is first cached in the buffer; a data selector selects the cached data by the index obtained through calculating the closest integer value of $F_s(T_N + \Delta T)/n$, wherein F_s is the sampling rate and k is the delay factor. The selected data is then outputted from the buffer and multiplied by a unit static vector ($e^{j2\pi/k}$). Finally, the multiplication result and the original sampled input waveform

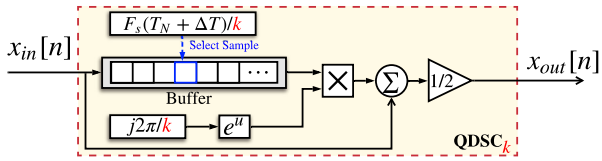

Fig. 4. Functional diagram of the proposed QDSC$_k$ algorithm.

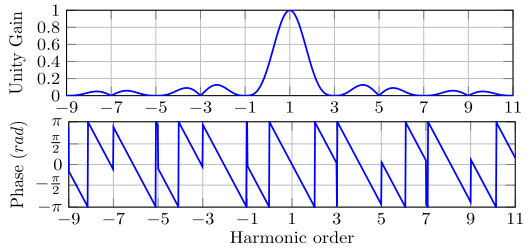

Fig. 5. Frequency response of the cascaded QDSC$_k$ with $k = [4, 4, 4, 8, 16, 32, 64]$.

at the current timestamp are summed and the output (x_{out}) of the QDSC module is reported.

The transfer function of a QDSC filter is defined by

$$H(f) = \frac{1}{2}\left[1 + exp\left(j\frac{2\pi}{k}\left(1 - (T_N + \Delta T)f\right)\right)\right]. \quad (16)$$

The value of k directly affects not only the buffer length and, consequently, the speed of the algorithm's dynamic response, but also the phasor measurement accuracy. Here, QDSC$_k$ with $k = [4, 4, 4, 8, 16, 32, 64]$ is selected and all QDSC modules are connected in cascade. As presented in the frequency response in Fig. 5, all odd harmonics except the positive fundamental frequency ($h = 1$) are eliminated, the gain for $h = 1$ is one, and no phase shift exists. Hence, this configuration extracts the positive-sequence fundamental phasor.

2) The Proposed M-Class SEA, Dynamic Gaussian-Weighted Least Square Taylor Series (GWT-M): Inaccurate estimation of ΔT in QDSC potentially hinders a stable frequency response and desired performance in (16). Therefore, a simplified Gaussian-weighted least square Taylor Series SEA introduce is introduced. Here the cached fundamental waveform is expressed as follows:

$$x_{ph,1}[n] \triangleq x_{ph,1}(nT_s) = \frac{1}{2}\vec{A}_{ph,1}[n]e^{j2\pi F_N nT_s} + \frac{1}{2}\vec{A}^*_{ph,1}[n]e^{-j2\pi F_N nT_s}, \quad (17)$$

where "$*$" denotes the conjugate operation, $\vec{A}_{ph,1}[n]$ is the static vector of the fundamental positive sequence at time slot n in the buffer, and $n = 0$ indicates the current time slot. With $n = 0, 1, 2, \ldots, N_{d\text{-}1}, N_d$, a queue of sampled x_{ph} with length N_d+1 is obtained in the buffer at the current time slot. Moreover, N_d must be an even number that guarantees an odd number of time slots in the buffer to estimate the phasors through the Taylor series. Meanwhile, the peak of the Gaussian window is located in the middle of the cached waveform. Therefore, the phasor estimation physically has a constant delay with $N_d/2$ time slots. To compensate the phase shift caused by this delay,

the evaluation in (17) turns to be

$$x_{ph,1}[n] = P[n] + P^*[n]$$
$$P[n] = e^{j2\pi F_N \frac{N_d}{2} T_s} \cdot \frac{1}{2}\vec{A}_{ph,1}[n] e^{j2\pi F_N n T_s} \quad (18)$$

The second-order Taylor polynomial of $\vec{A}_{ph,1}[n]$ is

$$\vec{A}_{ph,1}[n] = \vec{A}^{(0)}_{ph,1} + \vec{A}^{(1)}_{ph,1} \cdot \left(n - \frac{N_d}{2}\right) T_s + \vec{A}^{(2)}_{ph,1} \cdot \frac{(n - \frac{N_d}{2})^2 T_s^2}{2} \quad (19)$$

where, $\vec{A}^{(0)}_{ph,1}$, $\vec{A}^{(1)}_{ph,1}$, and $\vec{A}^{(2)}_{ph,1}$ are the zeroth, the first, and the second derivative of the static vectors of the fundamental positive sequence, which are evaluated at point $\frac{N_d}{2}$, respectively. The derivative of (19) gives out

$$\vec{A}'_{ph,1}[n] = \vec{A}^{(1)}_{ph,1} + \vec{A}^{(2)}_{ph,1}(n - \frac{N_d}{2})T_s. \quad (20)$$

Applying the Gaussian window, the three phasors and their conjugates are evaluated via the weighted least square as

$$\vec{\mathbf{A}} = (\mathbf{B}^{\mathcal{H}}\mathbf{G}\mathbf{B})^{-1}\mathbf{B}^{\mathcal{H}}(\mathbf{G} \cdot \mathcal{C}), \quad (21)$$

$$\vec{\mathbf{A}} = [\vec{A}^{(2)}_{ph,1}, \vec{A}^{(1)}_{ph,1}, \vec{A}^{(0)}_{ph,1}, \vec{A}^{*(0)}_{ph,1}, \vec{A}^{*(1)}_{ph,1}, \vec{A}^{*(2)}_{ph,1}]^{\mathcal{T}}, \quad (22)$$

$$\mathcal{C} = [x_{ph}[0],\ x_{ph}[1],\ x_{ph}[2],\ \ldots,\ x_{ph}[N_d]]^{\mathcal{T}}, \quad (23)$$

where $\mathbf{B}$ is a constant matrix of size $(N_d + 1) \times 6$ [51], and $\mathcal{C}$ is the cached original waveform samples in the proposed M-Class SEA buffer. $\mathbf{G}$ is the Gaussian weight of length $N_d + 1$. $\mathcal{H}$ is the Hermitian transpose.

With $\vec{\mathbf{A}}$ achieved in (22), the output of the suggested GWT-M algorithm can be assessed via (24)–(25):

$$A_m = |\vec{A}^{(0)}_{ph,1}|, \quad \Phi_m = \angle\vec{A}^{(0)}_{ph,1}, \quad F_m = F_N - \Delta f_m, \quad (24)$$

$$\text{ROCOF}_m = (-\Delta f_m[n] + \Delta f_m[n-1])/T_s, \quad (25)$$

$$\Delta f_m = Imag\{\vec{A}^{(1)}_{ph,1} \cdot e^{-j\angle\vec{A}^{(0)}_{ph,1}}\}/2\pi A_m T_s. \quad (26)$$

At this stage, ΔT can be evaluated in (27) and can be directly sent to the QDSC module.

$$\Delta T = \frac{\Delta f_m}{F_N^2 - \Delta f_m F_N} \quad (27)$$

As ROCOF from the proposed P-Class and M-Class SEAs is achieved through assessing the frequency derivatives, a low-pass filter (LPF) is needed to smoothen both the ROCOF_m and ROCOF_p estimation during disturbances.

V. Case Studies and Numerical Evaluations

A. Waveform Specifications, Configurations, and Assumptions

All the proposed modules share a sampling rate of 9.6 kHz. Mathematically, the wavelet transform should be able to cover the frequency range from 1 Hz to 3 kHz; the computing complexity of extracting such a frequency range could be reduced while sufficient feature extraction performance is ensured. In the proposed PCQ-WT design, the scaling factor a_k is selected from 1 to 256 and in a dyadic dilation manner, i.e., $a_k = 2^i$, wherein the exponent i is equally sampled within $[0, 8]$, i.e., pseudo-continuous. Considering the feature exaction performance (accuracy and speed), the wavelet length of 20 ms (192 time bins) is chosen. A fixed time shift factor $b_k = 96$ is used for simplicity. The buffered waveform length of 60 ms (576 time bins) is selected in (2). There is no padding during WT calculations and no congestion is assumed during data transfer or A2D conversion. Hence, the duration of each obtained scalogram is 40 ms, i.e., buffered waveform length (60 ms) subtracted with the wavelet length (20 ms).

The specifications of the test power waveforms are selected according to [13], [20] as detailed in Table I. The standard mathematical representations of the test input waveforms are defined as follows:

$$x(t) = X_m[1 + k_A u(t)] \times \cos(\omega_1 t + \phi_0) \quad (28a)$$
$$x(t) = X_m \times \cos[\omega_1 t + k_P u(t) + \phi_0] \quad (28b)$$
$$x(t) = X_m[1 + k_A \cos(\omega_m t)] \times \cos(\omega_1 t + \phi_0) \quad (28c)$$
$$x(t) = X_m \cos[\omega_1 t + k_P \cos(\omega_m t - \pi) + \phi_0] \quad (28d)$$
$$x(t) = X_m \cos[\omega_1 t + \pi R_f t^2 + \phi_0] \quad (28e)$$

(28a)–(28e) respectively, represent the magnitude jump, phase jump, amplitude modulation, phase modulation, and frequency ramp events; X_m and ϕ_0 are the amplitude and phase angle of the input signal; ω_1 is the nominal fundamental frequency of the system in rad/s; $u(t)$ is a unit step function. k_A and k_P are, respectively, the magnitude and phase factor in the modulation or step change events. $R_f = df/dt$ is the frequency ramp rate in Hz/s (a constant value in this test).

In total, eight types of waveforms are simulated corresponding to different grid operating conditions: (i) normal operating, (ii) magnitude step change, (iii) phase step change, (iv) harmonic distortion, (v) out-of-band interference, (vi) amplitude modulation (AM), (vii) phase modulation (PM), and (viii) frequency ramp. All test waveforms contain a Gaussian background noise with 40 dB signal to noise ratio (SNR).

B. Stage 1: Waveform Feature Extraction

The performance of the proposed PCQ-WT feature extraction module (Stage 1) is first examined in characterizing distinguishable patterns and signal signatures under a variety of grid operating conditions. For simplicity, the occurrence time of all demonstrated events is assumed the same.

1) Waveform Feature Extraction Under Transient Events: Several transient events are simulated and analyzed as follows: the magnitude step (Fig. 6(a)), the frequency step (Fig. 6(b)), and phase step (Fig. 6(c)). One can see that the proposed PCQ-WT pattern recognition algorithm has successfully recognized the unique peculiarities in the signals originated from such fast-transient events. Also, the signal patterns and signatures have appeared almost immediately as the events occur, making them absolutely suitable for online monitoring applications.

TABLE I
SPECIFICATIONS OF THE INPUT TEST WAVEFORM PARAMETERS

Test Name	Input Range	Test Name	Input Range
Magnitude Step	0.1–2pu	Phase Step	$\pm\pi/18$ radian
Harmonic Distortion	0.5%–10%THD; order up to 50^{th}	Out-of-Band Interference	10Hz to 120Hz; level 0.01–0.1pu
Amplitude Modulation	0.1Hz to 5Hz; level 0.005–0.1pu	Phase Modulation	0.1Hz to 5Hz; level 0.005–0.1pu
Frequency Ramp	$\pm$0.01Hz/s to $\pm$1Hz/s, within $\pm$5Hz	Normal Operation	N/A

*Signal to Noise Ration (SNR) of 40 dB is applied to all test signals.

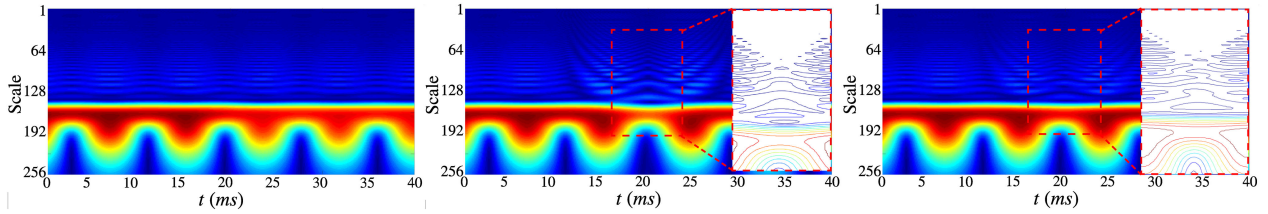

(a) Single-phase scalogram—magnitude step (b) Single-phase scalogram—frequency step (c) Single-phase scalogram—phase step

Fig. 6. Extracted features from simulated fast-dynamic transient events: (a)(d) magnitude step change of 0.2 pu at $t = 10$ ms; (b)(e) frequency step change of -2 Hz at $t = 10$ ms; (c)(f) phase step change of -10° at $t = 10$ ms.

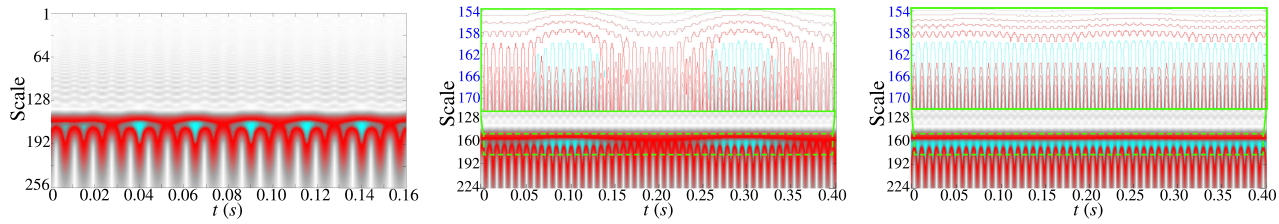

(a) Single-phase scalogram–Out-of-Band Interference (b) Single-phase scalogram—Amplitude Modulation (c) Single-phase scalogram—Phase Modulation

Fig. 7. Extracted features from simulated slow-dynamic steady-state events: (a)(d) out-of-band interference of 100 Hz at $t = 0.01$ s; (b)(e) amplitude modulation with magnitude of 0.05 pu and frequency of 5 Hz at $t = 0.04$ s; (c)(f) phase modulation with magnitude of 0.1 pu and frequency of 5 Hz at $t = 0.04$ s.

2) Waveform Feature Extraction Under Periodic Events: The following comparisons focus on the emergence of the slow-transient events with periodic impacts on power waveforms. The simulated events include out-of-band interference (Fig. 7(a)), amplitude modulations (Fig. 7(b)), and phase modulations (Fig. 7(c)), where the proposed PCQ-WT algorithm successfully extract unique features in the waveforms; such patterns convey important information on the underlying slow-dynamic events and provide a foundation based on which machine learning analytics and decision making platforms can operate in real-time.

C. Stage 2: Event Detection and Classification

1) Model Configuration: The CNN architecture design (e.g. the kernel size) is a relative empirical process [47]. In this paper, a common practice is followed, i.e., the kernel and pooling sizes are odd numbers and usually less or equal than seven [49]. Grid search is also conducted on searching through the depth and the learning rate of CNNs, as these two hyper-parameters impact the training performance the most. The range of the searched depth is $\{2, 3\}$ and the learning rates are $\{1 \times 10^{-2}, 1 \times 10^{-3}, \ldots, 1 \times 10^{-6}\}$. Here, only two depths are searched since the convolutional and pooling operation in the middle layers reduces the size of the output data, and the output of a 4-layer CNN is already small (8×8); a deeper network will lose all information of the input. Details of the proposed CNN architecture (e.g., the number of convolutional kernels) can be seen in Fig. 8; note that three CNNs sharing exact identical architecture are used for processing the three-phase scalograms. However, one-time training is needed only since the three phases are symmetric and can share one CNN using the same parameters. The proposed CNN analytics contain three convolutional layers (Conv1, Conv2 and Conv3), two max-pooling layers (MP1 and PM2) and two fully-connected layers (FC1 and FC2) with the following specifications: Input(256×385)–Conv1($100, 5\times11$)–MP1(3×3)–Conv2($100, 5\times5$)–MP2(3×3)–Conv3($64, 5\times5$)–FC1(600×1)–FC2(8×1). Scalograms are fed into the proposed analytics for a duration of 40 ms (385 data samples), which is treated as the observation window. Conventional images have homogeneous units on the horizontal and vertical axes, while the scalogram axes carry different information on either time or frequency. A wide kernel (5×11) in Conv1 that can extract more information from the transitions along the time axis is applied. The stride of Conv1 is (2,3), and Conv2 and Conv3 use strides with a size of (1,1). Except for FC1 layer,

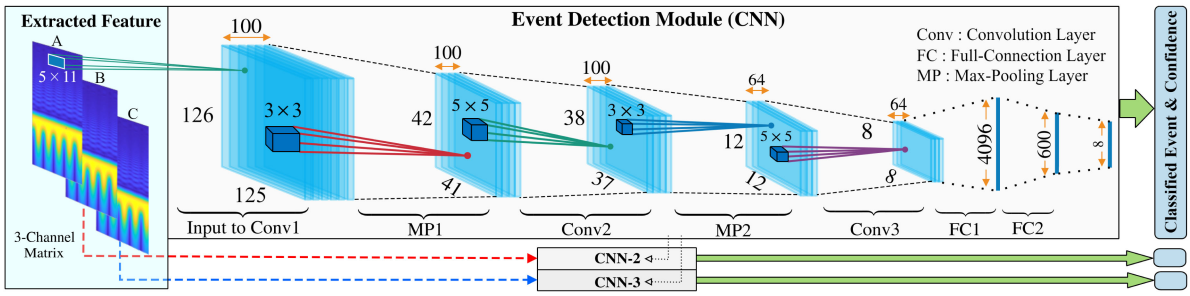

Fig. 8. Architectural diagram of the proposed CNN configuration with indicated parameters.

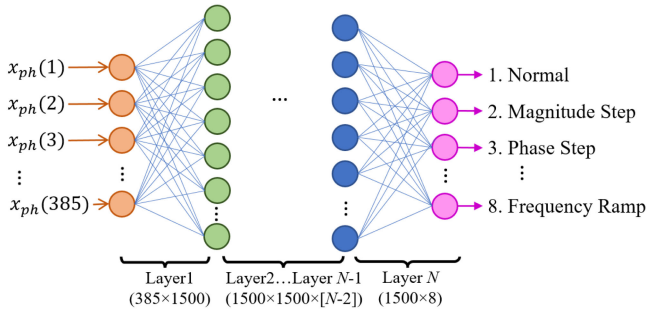

Fig. 9. The architecture of the compared MLP.

batch normalization is used in each convolutional and fully connected layers. In Conv3 and FC1, Dropout [52] is used to prevent over-fitting. Rectified Linear Units (ReLUs) are chosen as the activation function in the neural network. Cross-entropy is used as the loss function.

In this paper, 10,000 samples are generated per event for training the CNNs and another 1,000 samples of each event for validations. In each data sample, only one event occurs at a random time instant. If a generated scalogram contains the post-event phase-out stage, the new emerging event is then used for labeling this scalogram. During the training process, the CNNs are trained using the single-phase scalograms. Finally, another 1,000 samples per event type are generated for blind testing to verify the detection accuracy.

To explore the performance of the Multi-Layer Perceptron (MLP) and compare it against the suggested CNNs, the grid-search experiments on its architectures is also conducted. In the experiments of MLPs, the inputs are the original waveforms without any transformation; it is a 385-dimension vector. The depth of the networks and the learning rate are used in grid search. The range of the searched depth is $\{4, 6, 8 \ldots, 14\}$ and the learning rates are $\{1 \times 10^{-3}, 1 \times 10^{-4}, \ldots, 1 \times 10^{-6}\}$. The number of the perceptrons in the middle layers is fixed as 1,500 (see Fig. 9).

2) Offline Event Detection Accuracy: The event detection test results on a variety of events simulated offline are summarized in two confusion matrices presented in Fig. 10. The overall detection accuracy of the proposed mechanism using the single-phase scalograms is found 91.97% (see Fig. 10(a)). The best performance of MLPs is achieved by a 10-layer network and using a learning rate of 1×10^{-5} where the corresponding test accuracy is found to be 83.61%; Fig. 10(b) shows the confusion matrix of the test results. More importantly, MLP achieved a relatively lower classification accuracy; even worse, the number of parameters in this 10-layer MLP is about 16 million, while the suggested CNN has only 2.5 million parameters. The "true" label stands for the actual (simulated) test events, and the "predicted" label corresponds to the classification outcome of the proposed CNN modules. When inspecting the confusion matrix (Fig. 10(a)), one can find that the Amplitude Modulation vs Normal pair and Phase Modulation vs Frequency Ramp pair dominate the mis-classified examples (outliers). These two classes of events can overlap in real-world scenarios. For instance, if the modulation magnitude during the Amplitude Modulation event approaches zero, the distribution of the examples in this class approaches Normal. The similarity of the distribution between the Phase Modulation and Frequency Ramp events is mathematically proved in Appendix III (see [41]). Furthermore, one ultimate goal of classification in the proposed framework is to facilitate the right selection of the SEAs. These miss-classified events share similar behavior, which would not considerably impact the measurement accuracy.

3) Online Event Classification Application: The previous analysis verified the promising accuracy of the proposed event detection scheme. Here, online experiments on the integrated feature extraction and event detection mechanisms are conducted in a workstation which has an Intel Core i7-9700 K CPU and Nvidia GeForce GTX 2080Ti GPU. Note that the feature extraction module takes approximately 1.20 ± 0.23 ms to operate and the event classification engine through CNN takes approximately 1.04 ± 0.31 ms to generate the outcome. As the total operation time of the proposed event detection mechanism is 2.24 ± 0.39 ms, the proposed mechanism suites well the real-time event detection applications.

To demonstrate the online classification performance of the proposed analytics, a synthetic waveform with a Phase Step event occurring at $t = 0$ s is fed into the feature extraction and event detection module. In order to avoid possible congestions, the event detection is executed in a rolling manner, where the length of the rolling past observation (execution interval) is set to be every 4 ms, which is larger than the combined processing time. The result is shown in Fig. 11. One can see that it took approximately 20 ms for the proposed scheme to correctly detect the event using Phase A waveform. It can be also noticed in Fig. 11 that an event classification delay and a residual effect

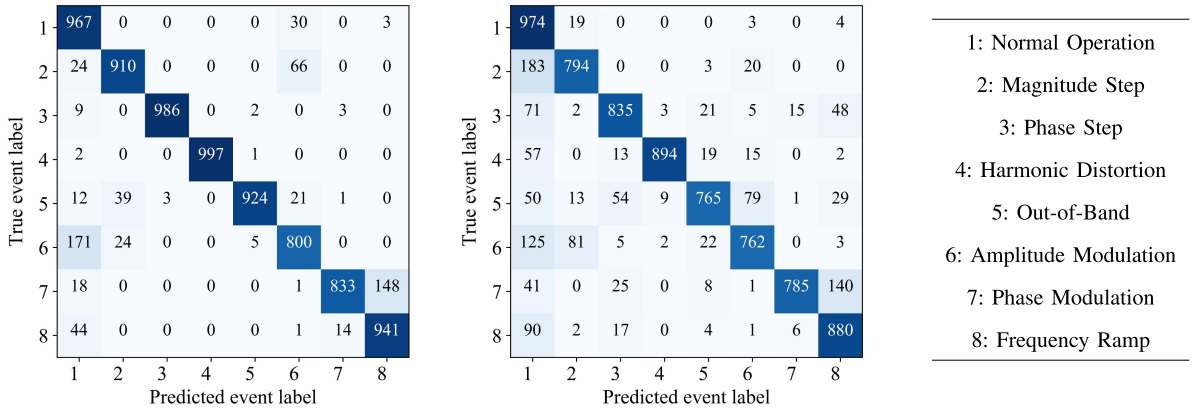

(a) The Proposed CNN (b) MLP (c) Event Index

Fig. 10. Test results of the proposed CNN engine and MLP; detection accuracy is presented in the confusion matrix.

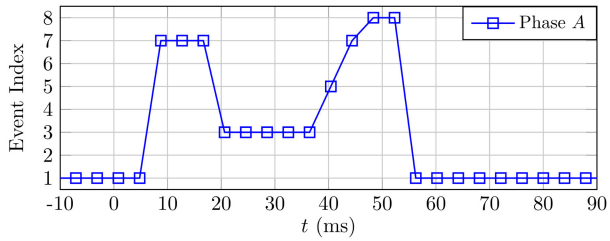

Fig. 11. Online event classification test results: phase step event occurs at $t = 0$ ms (Event indexes are shown in Fig. 10(c)).

after the event ends do exist. The reason lies in the fact that the event is hard to be classified before the corresponding patterns and signal signatures fully move into the observation window. Similarly, when the patterns start phasing out of the observation window but before they fully vanish, the classification outcome is found unstable. However, it is still preferable to accurately detect and classify the new emerging event before the corresponding features fully appear in the observation window, and such inaccuracies in the output only last for 20 ms, i.e., 1.2 fundamental cycles; this delay is still within the desirable limits and acceptable. Meanwhile, it can be seen in all figures in Section V-B that the center of signal signatures resulted from the fast-dynamic transient events can be observed after 10 ms of the occurrence. With a conservative estimation, the fingerprint of the event can be generally revealed and classified after one fundamental cycle (16.67 ms) plus 2.24±0.39 ms, which is approximately 20 ms. Therefore, the proposed event classification scheme can meet the standard granularity limits [13] and achieves the desired performance requirements for real-time applications.

D. Stage 3: Adaptive SEA Selection

In order to achieve high-fidelity synchrophasor measurements at all times, one need to know which SEA best suits a certain type of event or grid operating condition. The proposed framework for adaptive SEA selection houses multiple installed SEAs, the outputs of which could be adaptively selected as needed; therefore, multiple SEAs are analyzed to demonstrate their different performances. A dynamic Quadrature Delayed Signal Cancellation SEA for high-speed P-Class applications (QDSC-P) and a Gaussian Weighted Taylor Series least square SEA for high-accuracy M-Class applications (GWT-M) are proposed in Section IV-D. An "enIpDFT" SEA [19] and a P- and M-Class SEA from [53] which are named as "P & M" are also included. Here, the enIpDFT is categorized as a P-Class SEA due to its high response speed verified and reported in [19]. When implementing the P & M SEA, P & M-P and P & M-M are used to represent the functionalities corresponding to P-Class and M-Class applications, respectively. The two SEAs are primarily used for performance comparison with our proposed QDSC-P and GWT-M SEAs. All SEAs sharing the same sampling rate of 9.6 kHz.

1) Model Configurations and Parameter Settings: The GWT-M SEA possesses a Gaussian window with a length of 4.8 fundamental cycles and the shape factor $\alpha = 3.6$; the enIpDFT SEA is characterized via a Hann window with a length of 3 fundamental cycle—the same as that utilized in [19]. The P & M-P and P & M-M SEAs use a Kaiser window of length 3.8 and 5.8 fundamental cycles, respectively [53]. Additionally, filtering the noise and the distortion in ROCOF measurement by higher-order low-pass filters (LPFs) can significantly reduce the ROCOF error (RFE). This, in turn, results in a slower ROCOF measurement. In order to ensure a fair performance comparison of different SEAs when assessing ROCOF, an LPF with the following transfer function is applied when needed:

$$h(z) = \frac{0.0968z + 0.0968}{z - 0.8063}, \tag{29}$$

This applied setting ensures an acceptable dynamic response speed within the maximum RFE limits as enforced in [13].

2) Steady-State Compliance Tests: Due to space limitations and in accordance with the IEEE standard [13], the results on only one steady-state compliance test—frequency sweeping—is plotted in Fig. 12, while additional test results can be found in Appendix II.A [41]. When the test signal frequency changes from 55 Hz to 65 Hz, the maximum Total Vector Errors (TVEs)

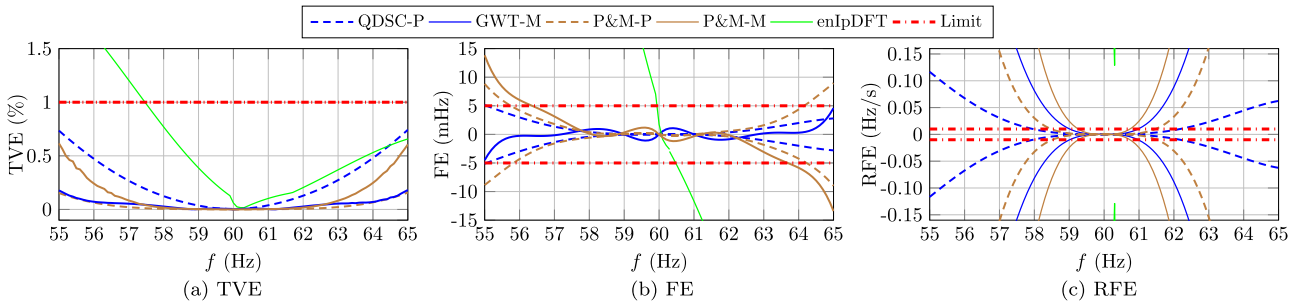

Fig. 12. Performance evaluation of different SEAs under Frequency Sweeping tests.

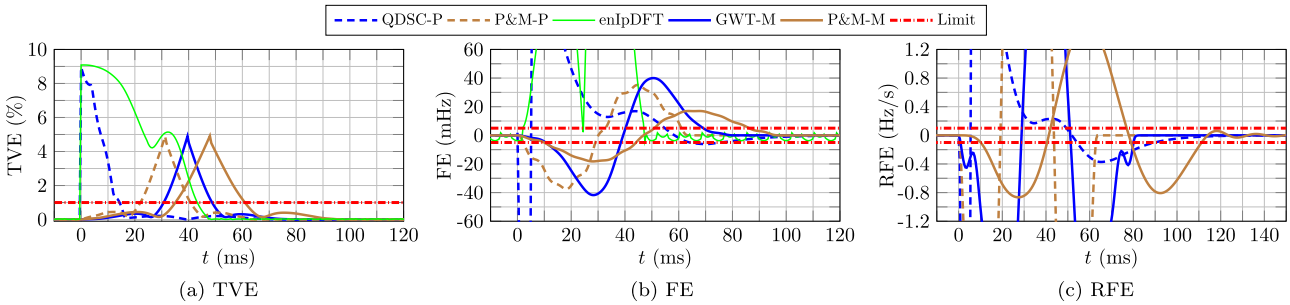

Fig. 13. Performance evaluation of different SEAs under Magnitude Step test of 0.1 pu.

for all SEAs within the proposed framework are assessed and plotted in Fig. 12(a). One can see that the outputs from all SEAs result in TVE measures less than 1%, except the enIpDFT (solid green line) whose TVE exceeds the 1% threshold when the frequency is less than 57.5 Hz.

For the P-Class SEAs, the Frequency Error (FE) limit is set to 10mHz according to [13]. The proposed QDSC-P (dashed blue line) in Fig. 12(b) is observed to reach its maximum FE ($\pm$5mHz) at $f = 55$ Hz. For enIpDFT SEA, the FE stays within the limit only when f is around the nominal frequency and it quickly exceeds the 5mHz limit when $f \leq$59.7 Hz and $f \geq$60.9 Hz; therefore, the FE results in Fig. 12(b) reveal that the P-Class enIpDFT SEA fails the conducted tests in the required frequency range from 58 Hz to 62 Hz. When focused on FE, the results demonstrate that the proposed QDSC-P outperforms the other two SEAs. The P & M-P SEA (dashed brown line) stays within the limits when the off-nominal frequency is beyond $\pm$4.15 Hz, which satisfies the standard requirement. In the M-Class FE plot of Fig. 12(b), our proposed GWT-M SEA (solid blue line) stays within the M-Class FE limit (5mHz) when f is in the designated range, but P & M-M fails when $f >$63.6 Hz or $f <$56.3 Hz.

Fig. 12(c) illustrates the RFE performance comparison of the integrated SEAs within the smart sensor. One can see from the numerical test results that only the proposed QDSC-P SEA satisfies the P-Class standard requirement (RFE $\leq$0.01 Hz/s) at the frequency range from 58 Hz to 62 Hz. The RFE corresponding to the P& M-P SEA exceeds the desired limit when $f >$61.5 Hz or $f <$58.5 Hz. In addition, the reported RFE for the enIpDFT SEA fails the compliance thresholds in the entire frequency range tested. For the other two M-Class SEAs, both the proposed GWT-M and P & M-M fail to meet the standard requirements, as the corresponding RFEs quickly exceed the limit when the off-nominal frequency is 0.7 Hz and 1.0 Hz, respectively. However, the proposed GWT-M SEA performs better than the P & M-M SEA, as the former can tolerate a wider off-nominal frequency range.

3) Dynamic Compliance Tests: The dynamic response of different SEAs is tested to verify their compliance with the standard requirements. Magnitude Step Tests are here focused as presented in Fig. 13(a), while additional dynamic test results are provided in Appendix II.B [41]. In Fig. 13(a), one can see that the TVE indicator corresponding to the QDSC-P SEA offers the fastest convergence speed (13 ms) when the magnitude step of 0.1pu occurs. The P & M-P SEA takes 40 ms to return below the limit (which is more than two times of that for the QDSC-P SEA) and fails to meet the standard requirement of $1.7/f_0 =$ 28.3 ms. Both M-Class SEAs achieve the standard compliance requirement of the TVE response time limit (79 ms). Fig. 13(b) illustrates the FE comparisons of different SEAs. The enIpDFT SEA is found the fastest (taking only 46 ms) to return below the desired FE limit, while this time is 60 ms and 82 ms for the P & M-P and QDSC-P SEAs, respectively. Unfortunately, both QDSC-P and P & M-P SEAs take longer than the desired $3.5/f_0 = 58.3$ ms response time limit. The GWT-M SEA takes 70 ms and the P & M-M SEA takes 85 ms to converge, which are within the 120 ms prescribed response time limit in [13]. With a focus on the RFE indicator, the enIpDFT SEA fails to meet the standard requirement and, hence, is not included in the results presented in Fig. 13(c). The QDSC-P SEA fails the magnitude step test as it violates the P-Class RFE response time limit ($4/f_0 = 66.6$ ms). Since removing the LPF would not improve the ROCOF response speed of the QDSC-P SEA, it is

TABLE II
BEST-FIT SEAS FOR PHASOR MEASUREMENT UNDER DIFFERENT TEST SCENARIOS AND OPERATING CONDITIONS

	C†	Phasor	Frequency	ROCOF
Normal Frequency	P	P&M-P		
	M	GWT-M		
Abnormal Frequency	P	P&M-P	QDSC-P	
	M	GWT-M		
Harmonic Distortion	P	QDSC-P		
	M	GWT-M		
Out-of-Band Interference	M	P&M-M	GWT-M	
Phase Modulation	P	P&M-P		QDSC-P
	M	GWT-M		P&M-P
Amplitude Modulation	P	P&M-P		
	M	GWT-M		
Frequency Ramp	P	P&M-P	QDSC-P	
	M	GWT-M		
Magnitude Step	P	QDSC-P	P&M-P	
	M	GWT-M		
Phase Step	P	P&M-P	enIpDFT	P&M-P
	M	GWT-M		

†PMU Class.

concluded not suitable for ROCOF measurements, particularly, during dynamic test conditions. The P & M-P SEA takes 63 ms to return back to the RFE limit which satisfies the standard response time requirement. Compared to the GWT-M SEA, the P & M-M SEA shows the slowest RFE convergence speed, but is still within the 129 ms M-Class response time limit under dynamic test conditions. Hence, the proposed GWT-M SEA is concluded as the most promising candidate for M-Class ROCOF measurements.

4) SEA Selection Strategies: The analyzed SEA test results verified that different SEAs perform differently under various test scenarios and simulated operating conditions. The proposed approach to synchrophasor measurement is, hence, adaptive in that only the best-fit SEAs are activated at any time instant, thereby ensuring high-fidelity measurements. The results are demonstrated in Table II, offering a holistic view on the performance and advantage of each SEA with regards to different performance metrics of interest. The results presented in this table can be used for adaptively selecting an SEA according to the detected event. Meanwhile, one can see in Table II that the proposed QDSC-P and GWT-M SEAs are the best choice in 2/3 (i.e., 34 out of 51) of scenarios, which confirms their effectiveness in improving the synchrophasor measurements. Moreover, the tests conducted in Section V-C verified that the proposed adaptive SEA selection mechanism can ensure the desired accuracy and speed requirements of different end-use applications that utilize the synchrophasor measurements. Note that the proposed adaptive mechanism is generic enough to accommodate other SEAs that are not investigated here but of interest to the user.

E. Integrated Online Test

An integration of the suggested SEA selection mechanism in conjunction with the event detection and classification modules is demonstrated in Fig. 14. With the occurrence of a Harmonic Distortion event in the waveforms and following a transition period (as marked in red), the SEA selection mechanism selects

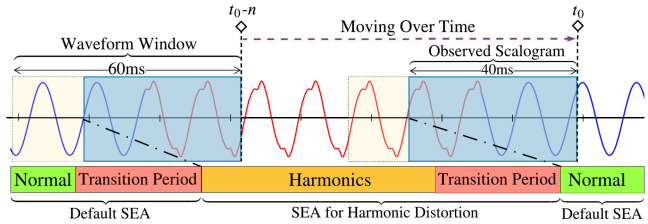

Fig. 14. An example integration of the online event classification jointly with the SEA selection functions during a harmonic distortion event.

the best-fit SEA and achieves the high-fidelity measurements under the detected event. When the Harmonic Distortion event disappears, and the corresponding waveforms return back to normal, it takes another transition period to switch the SEA back to most suitable one for synchrophasor measurements under normal operating condition. One may notice that phase-out misclassifications do exist in Fig. 14, and they could be observed during the "transition period". This is because the event is hard to be classified before the corresponding patterns and signal signatures fully move into the observation window. Similarly, when the patterns start phasing out of the observation window but before they fully vanish, the new emerging event could be misclassified.

In order to demonstrate the feasibility of implementing the suggested approach and verify the performance and robustness of the proposed event detection and SEA selection mechanisms during both steady-state and dynamic events, three experiments are conducted:

1) A synthetic waveform containing multiple events at different designated time instants is generated and fed into the smart sensor. The detected event with confidence rates and the selected P-class TVE output are recorded. Meanwhile, the TVEs for all the embedded P-class SEAs are recorded for comparison.
2) A grid-connected three-phase inverter in Typhoon-HIL402 is used as the simulation platform. The voltage waveform from Phase A is captured, down sampled, and then fed into the smart sensor. This waveform contains a capacitor filter loss event. The detected event with confidence rates and the selected P-class FE output is recorded. Also, it is known that the frequency is fixed at 60 Hz. The FE indicators for all P-class SEAs are recorded for comparison.
3) A synthetic waveform (used for testing the CNN in Fig. 11) containing 5° phase step at $t = 0$ sec is re-generated and fed into the smart sensor. The detected event with confidence rates and the selected P-class TVE output as well as all three P-class TVEs are reported.

In the designed integrated Test 1 and Test 2, and for simplicity in assembling each module into one integrated system, the CNN is complied into CPU and the computing process of both WT and CNN are assigned in one single core of the Intel I7-9700 k. The average time for WT and CNN computations in CPU is 7.72±0.22 ms; therefore, the rolling past observation (execution interval) is conservatively set to be every 13 ms when using

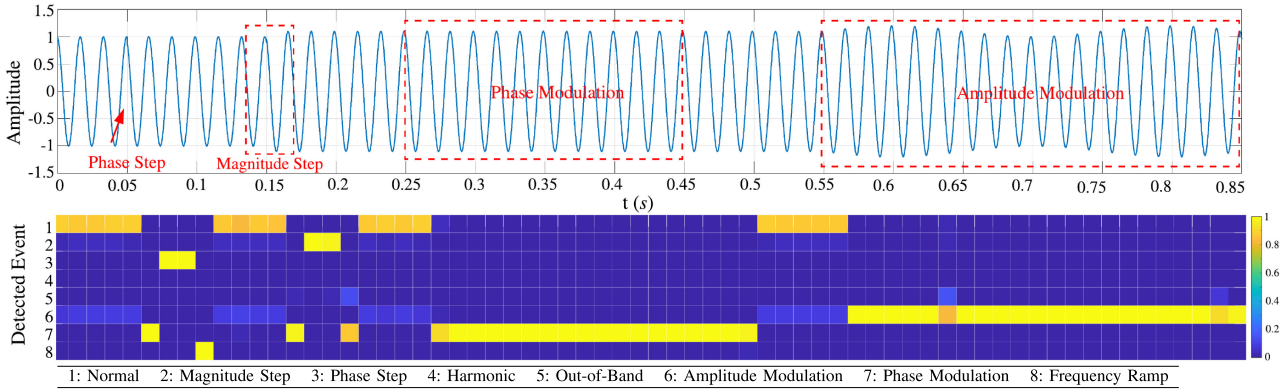

(a) Simulated waveform and event detection outcomes of the proposed framework

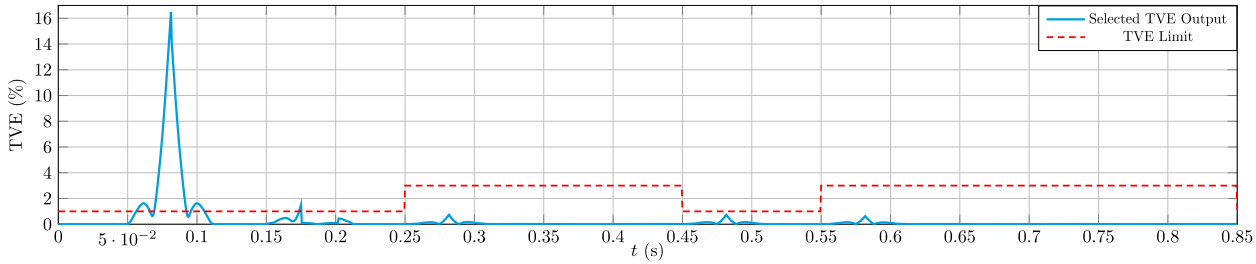

(b) Output TVE with adaptive SEA selection

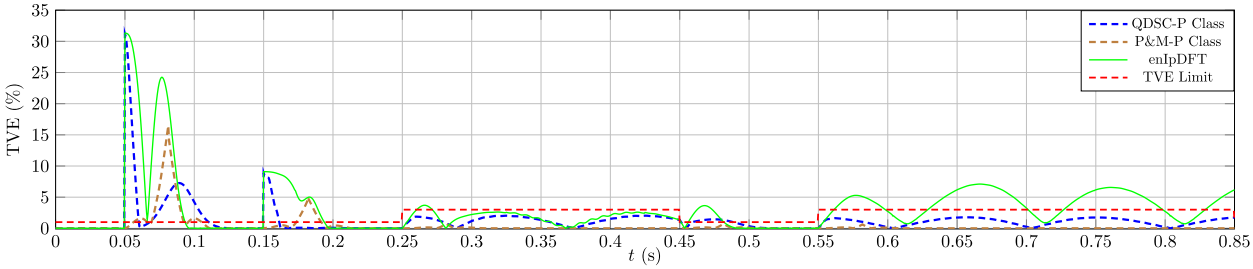

(c) Output TVE for each individual P-class SEA

Fig. 15. Online event detection and measurement fidelity test results: Test Case 1.

CPU. Note that using a GPU significantly reduces the processor time (2.24±0.39 ms, 70% faster than CPU) and the execution time (4 ms); thus, it would be necessary to use GPU for the entire process to be computationally-efficient in real-time applications. To demonstrate the proposed event detection method in a higher time resolution, the feature extraction and event detection process is performed in GPU in Test 3 with execution interval 4 ms, but the SEA selection functionality is still performed in CPU. Additionally, to demonstrate the robustness of our approach in providing accurate (correct) detection results under malicious cyber-attack scenarios, it is here assumed that the incoming GPS timing and communication signals are lost or jammed by a cyber intruder in both test cases. Therefore, only the inner timing clock is available in the smart sensor. Meanwhile, the local operator can rely solely on the smart sensor solution and read its output to monitor the operating condition where the sensor is installed.

1) Test Case 1: The synthetic waveform can be seen on the upper side of Fig. 15(a), below which is the heat-map representing the event detection results over time, where the classification confidence is marked with colors along the time axis. The event featured with the highest confidence is finally reported throughout the simulated waveform. In this example, all events are correctly detected. Similar to the measurement delays in SEAs, the detection delay is inevitable due to the waveform buffer. The worst detection delay is found to be approximately 50 ms. The post-event phase-out miss-classifications do also exist and can be observed during the transitions from *Normal* to *Phase Step* conditions and *Phase Step* returning back to *Normal* operating state. Similar observations can be also found on the *Magnitude Step* event. The miss-predicting labels would result in a sub-optimal selection of the SEAs and increase the measurement errors in some of the outputs compared to those obtained when the events are correctly detected.

Fig. 15(b) and Fig. 15(c) demonstrate the output TVEs when the adaptive SEA selection is applied and individually for all embedded P-class SEAs, respectively. One can see that the proposed adaptive SEA selection mechanism has chosen the lowest-TVE SEA (i.e., P&M-P) during the *Phase Step* event observation. Regarding the *Magnitude Step* event, the TVE output corresponds to the P&M-P and the proposed CDSC-P, which

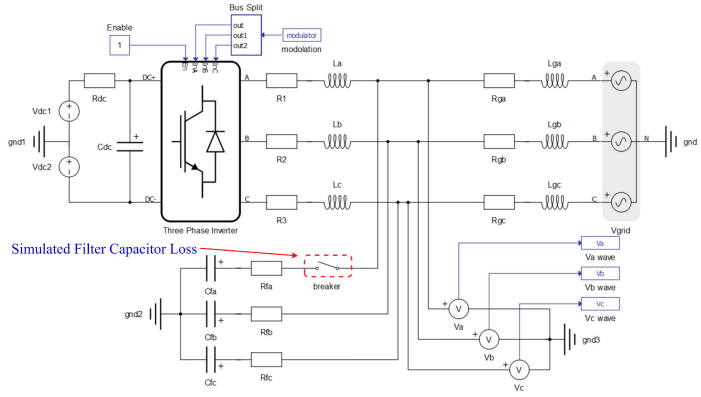

(a) Typhoon-HIL-based virtual inverter model.

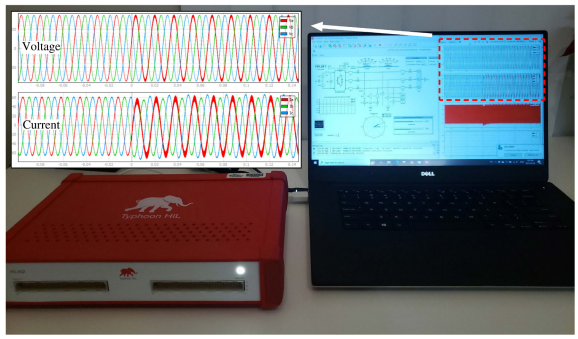

(b) Typhoon-HIL402 simulation platform

Fig. 16. Power electronic model configuration and the simulation platform.

is the lowest among all TVEs reported in Fig. 15(c). Similarly for the *Phase Modulation* and *Amplitude Modulation* events, the TVE from the selected P&M-P is the smallest; however, spikes can be observed even through there is no sudden change in the waveform. Therefore, a well-selected set of SEAs is necessary for the operation of the smart sensor in the future. This test example demonstrated the effectiveness of the proposed analytics within a smart sensor technology. The operator can quickly identify the low frequency oscillation events at the measurement point via the smart sensor solution, even without any established communications between the substations and the control center.

Regarding the event detection errors, one can find that in most cases, the miss-predicted events would share the same SEA output as the actual event (see Table II). For example, the TVEs reported for the *Phase Step* and *Phase Modulation* events share the same SEA; in such cases, the miss-prediction would not affect the measurement accuracy (see Fig. 15(b) and Fig. 15(c)). Also, the miss-predicted events usually occur in dynamic transient states, where the features corresponding to the incoming event are not yet fully observed; hence, a small number of miss-predicting labels would not harm the post event analysis. Finally, the CNN classifier not only outputs the predicted classes of the prevailing events, but also provides the confidence of the event classification outcome (see Fig. 15(a)); while the predictions may miss the ground truth at the beginning or the end of the event duration, the confidence rate offers more information on the fidelity of the decisions.

2) Test Case 2: A grid-connected three-phase inverter shown in Fig. 16(a) is simulated in Typhoon-HIL402, in which a filter capacitor loss event is to be tested. Fig. 16(b) illustrates the captured waveform in this test. For simplicity, the waveform is cropped and the filter capacitor loss event is assumed to occur at $t = 100$ ms. The cropped waveform is fed into the proposed smart sensor framework. From Fig. 17(a), one can notice that the FE corresponding to the P&M-P SEA is selected as the output during the normal condition. Once the filter capacitor loss occurs at Phase A, the confidence rate for the *Normal* operating condition dropped, and a *Harmonic distortion* event was reported around 30 ms later. Even out-of-band inference can

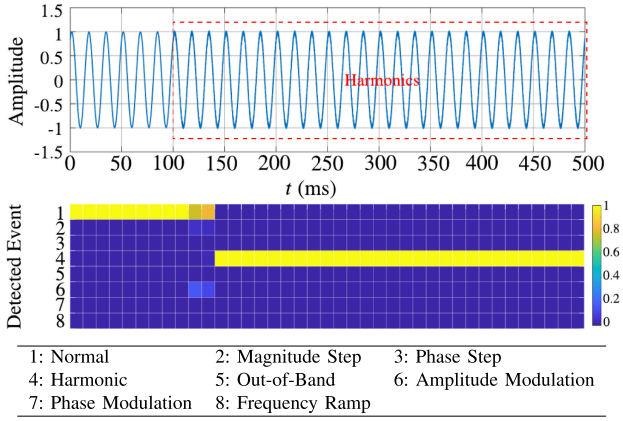

(a) Voltage waveform and event detection outcomes of the proposed framework

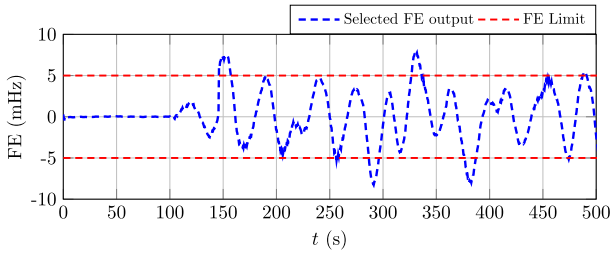

(b) Output FE with adaptive SEA selection

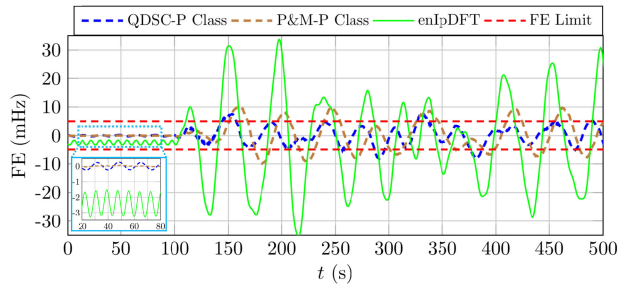

(c) Output FE for each individual P-class SEA

Fig. 17. Online event detection and measurement fidelity test results: Test Case 2.

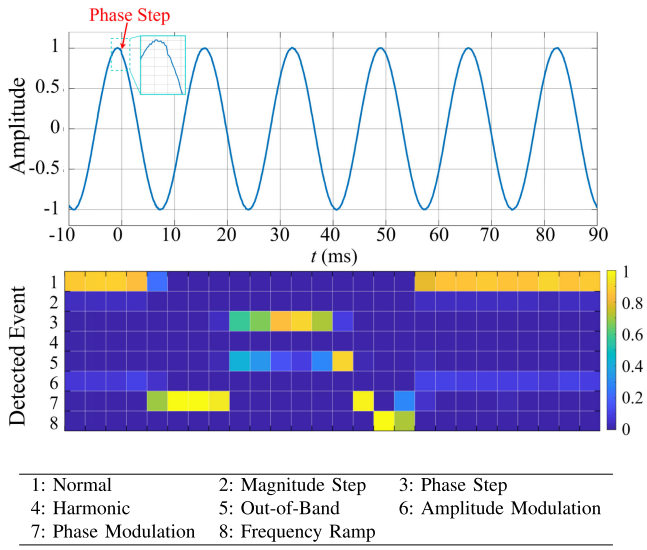

(a) Voltage waveform and event detection outcomes of the proposed framework

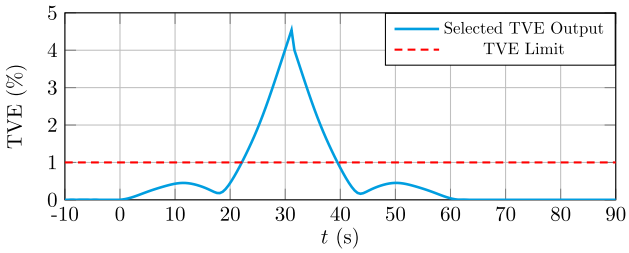

(b) Output TVE with adaptive SEA selection

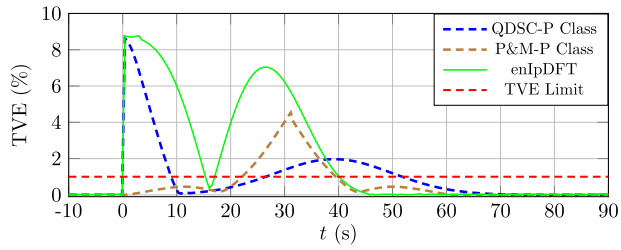

(c) Output TVE for each individual P-class SEA

Fig. 18. Online event detection and measurement fidelity test results: Test Case 3.

be observed in the spectrum, and the harmonics still dominated. Therefore, the performance of the proposed event detection module is confirmed to be desirable in this test. Moreover, before the correct event is reported, the distortions in the FE plot are observed to be trending higher but still remaining within the desirable limits. The smallest FE output was then selected after the harmonic event was identified. The FE limit violation is reduced compared to that observed from other SEAs in Fig. 17(c).

In this test, a practical application for detecting the abnormal harmonics in the case of communication failures and loss of GPS timing signal was demonstrated. Conventional PMUs rely on communication channels and common GPS timing to provide valid phasor measurements for control center analytics, yet vulnerable to delays and failures. With the assistance of the proposed smart sensor solution, harmonic distortion was detected and reported locally; meanwhile, the best-fit SEA that minimizes the measurement errors during different operating conditions and in presence of a variety of events is dynamically selected. Thus, the operator can then be aware that Phase A of the inverter could be operating in a degraded condition, even though the frequency and phasor magnitudes are still within the nominal range (varying between 60.005 Hz to 59.995 Hz). The operator can start to pinpoint the potential causes of the harmonics, then to quickly identify and replace the lost filter capacitor to ensure the quality of the distributed power to the customers. This operation can be also performed even if an adversarial cyber attacker blocks the communication channels.

3) Test Case 3: In Test 3, the test waveform used in Fig. 11 is re-generated and presented in Fig. 18(a). The confidence rates indicated the detailed event detection results that are demonstrated in Fig. 11. Also, these confidence rates are reported with a higher time resolution compared to Test 1 and Test 2. Similar to the phase step event detection results shown in Test 1, the initial detection outcome during this phase step event moving into the observation window is *Phase Modulation*. Then, the true event, i.e., the *Phase Step* is reported. Finally, the phase-out stage is misclassified as *Frequency Ramp*. However, this similar combination of these three detected events (Phase Modulation-Phase Step-Frequency Ramp) can be used as an indicator to determine the actual occurrence of the Phase Step event from a series of event detection results. This high-resolution test result highlights the benefits of a shorter execution interval with the assistance of GPU. The SEA selection model still provides promising results as it was also demonstrated in Test 1 and Test 2 (see Fig. 15(b) and Fig. 17(b), respectively).

VI. Conclusion

This paper presented innovative data-driven analytics embedded in a smart sensor solution technology; the proposed solution transforms the existing centralized monitoring and control paradigms to distributed intelligence for online situational awareness in power grids. Furthermore, the proposed framework is equipped with an adaptive SEA selection mechanism that ensures high-fidelity synchrophasor measurements continually under a variety of events. This paper numerically analyzed and verified the performance of different modules within the presented technology: online feature extraction, event detection and classification as well as adaptive measurements. Through extensive testing and analyses, it was concluded that (i) the proposed event detection and classification scheme using machine learning could provide real-time, accurate, and informative guidelines on the ongoing operating conditions in power grids, thereby facilitating automatic control actions in response; (ii) different SEAs perform differently under different events and operating conditions in the grid; with the knowledge on the performance of different P-Class and M-Class SEAs under various grid operating conditions, the best-fit SEA output is selected in an automated manner for high-fidelity measurements.

The proposed analytics are based on a data-driven approach, thus heavily relying on the credibility of the waveform dataset. Future research may focus on investigating other solutions for dealing with datasets including multiple simultaneous events as well as training and testing the proposed solution using real-world waveforms containing such events. Also, the tests of the proposed solution working jointly with actuation and/or control devices and quantification of the misclassification impacts on power system operation need to be further researched.

REFERENCES

[1] J. A. de la O Serna, "Synchrophasor measurement with polynomial phase-locked-loop Taylor-Fourier filters," *IEEE Trans. Instrum. Meas.*, vol. 64, no. 2, pp. 328–337, Feb. 2015.

[2] M. Bertocco *et al.*, "Compressive sensing of a Taylor-Fourier multifrequency model for synchrophasor estimation," *IEEE Trans. Instrum. Meas.*, vol. 64, no. 12, pp. 3274–3283, Dec. 2015.

[3] T. Becejac, P. Dehghanian, and M. Kezunovic, "Analysis of PMU algorithm errors during fault transients and out-of-step disturbances," in *Proc. IEEE PES Transmiss. Distrib. Conf. Expo.-Latin Amer.*, 2016, pp. 1–6.

[4] N. H. Abbasy and H. M. Ismail, "A unified approach for the optimal PMU location for power system state estimation," *IEEE Trans. Power Syst.*, vol. 24, no. 2, pp. 806–813, May 2009.

[5] S. Chakrabarti, E. Kyriakides, and D. G. Eliades, "Placement of synchronized measurements for power system observability," *IEEE Trans. Power Del.*, vol. 24, no. 1, pp. 12–19, Jan. 2009.

[6] M. H. Rezaeian Koochi, P. Dehghanian, S. Esmaeili, P. Dehghanian, and S. Wang, "A synchrophasor-based decision tree approach for identification of most coherent generating units," in *Proc. Annu. Conf. IEEE Ind. Electron. Soc.*, Oct. 2018, pp. 71–76.

[7] D. Macii, D. Petri, and A. Zorat, "Accuracy analysis and enhancement of DFT-based synchrophasor estimators in off-nominal conditions," *IEEE Trans. Instrum. Meas.*, vol. 61, no. 10, pp. 2653–2664, Oct. 2012.

[8] S. Wang, A. Etemadi, and M. Doroslovački, "Adaptive cascaded delayed signal cancellation for three-phase grid under unbalanced and distorted condition," *Electric Power Syst. Res.*, vol. 180, pp. 1–13, 2020.

[9] J. Liu, F. Ni, P. A. Pegoraro, F. Ponci, A. Monti, and C. Muscas, "Fundamental and harmonic synchrophasors estimation using modified Taylor-Kalman filter," in *Proc. IEEE Int. Workshop Appl. Meas. Power Syst.*, 2012, pp. 1–6.

[10] V. V. Terzija, M. B. Djuric, and B. D. Kovacevic, "Voltage phasor and local system frequency estimation using Newton type algorithm," *IEEE Trans. Power Del.*, vol. 9, no. 3, pp. 1368–1374, Jul. 1994.

[11] M. Chen, L. Peng, Q. Zhao, X. Zou, X. Wang, and X. Wei, "Positive sequence detector based on cascaded delayed quadrature signal cancellation," in *Proc. IEEE Energy Convers. Congr. Expo.*, Sep. 2015, pp. 1089–1094.

[12] S. Golestan and J. M. Guerrero, "Conventional synchronous reference frame phase-locked loop is an adaptive complex filter," *IEEE Trans. Ind. Electron.*, vol. 62, no. 3, pp. 1679–1682, Mar. 2015.

[13] *IEEE/IEC International Standard - Measuring Relays and Protection Equipment - Part 118-1: Synchrophasor for Power Systems - Measurements*, IEC/IEEE 60255-118-1:2018, pp. 1–78, 2018.

[14] A. Z. Amanci and F. P. Dawson, "Synchronization system with zero-crossing peak detection algorithm for power system applications," in *Proc. Int. Power Electron. Conf.*, 2010, pp. 2984–2991.

[15] S. Das and T. Sidhu, "Robust algorithm to estimate fault synchrophasor from fault-transient synchrophasor in phasor data concentrator," *IET Gener., Transmiss. Distrib.*, vol. 9, no. 2, pp. 124–132, 2015.

[16] Á. Ortega and F. Milano, "Comparison of different PLL implementations for frequency estimation and control," in *Proc. 18th IEEE Int. Conf. Harmon. Qual. Power*, 2018, pp. 1–6.

[17] P. K. Dash, K. R. Krishnanand, and M. Padhee, "Fast recursive Gauss-Newton adaptive filter for the estimation of power system frequency and harmonics in a noisy environment," *IET Gener., Transmiss. Distrib.*, vol. 5, no. 12, pp. 1277–1289, Dec. 2011.

[18] A. J. Roscoe, I. F. Abdulhadi, and G. M. Burt, "P and M class phasor measurement unit algorithms using adaptive cascaded filters," *IEEE Trans. Power Del.*, vol. 28, no. 3, pp. 1447–1459, Jul. 2013.

[19] P. Romano and M. Paolone, "Enhanced interpolated-DFT for synchrophasor estimation in FPGAs: Theory, implementation, and validation of a PMU prototype," *IEEE Trans. Instrum. Meas.*, vol. 63, no. 12, pp. 2824–2836, Dec. 2014.

[20] T. Becejac, P. Dehghanian, and M. Kezunovic, "Probabilistic assessment of PMU integrity for planning of periodic maintenance and testing," in *Proc. IEEE Int. Conf. Probabilistic Methods Appl. to Power Syst.*, 2016, pp. 1–6.

[21] R. K. Mai, L. Fu, Z. Y. Dong, B. Kirby, and Z. Q. Bo, "An adaptive dynamic phasor estimator considering DC offset for PMU applications," *IEEE Trans. Power Del.*, vol. 26, no. 3, pp. 1744–1754, Jul. 2011.

[22] J. Ren and M. Kezunovic, "An adaptive phasor estimator for power system waveforms containing transients," *IEEE Trans. Power Del.*, vol. 27, no. 2, pp. 735–745, Apr. 2012.

[23] I. Kamwa, S. Samantaray, and G. Joos, "Wide frequency range adaptive phasor and frequency PMU algorithms," *IEEE Trans. Smart Grid*, vol. 5, no. 2, pp. 569–579, Mar. 2014.

[24] C. Qian and M. Kezunovic, "A power waveform classification method for adaptive synchrophasor estimation," *IEEE Trans. Instrum. Meas.*, vol. 67, no. 7, pp. 1646–1658, Jul. 2018.

[25] G. Klein, B. Moon, and R. R. Hoffman, "Making sense of sensemaking 1: Alternative perspectives," *IEEE Intell. Syst.*, vol. 21, no. 4, pp. 70–73, Jul./Aug. 2006.

[26] M. Panteli, P. A. Crossley, D. S. Kirschen, and D. J. Sobajic, "Assessing the impact of insufficient situation awareness on power system operation," *IEEE Trans. Power Syst.*, vol. 28, no. 3, pp. 2967–2977, Aug. 2013.

[27] M. Panteli and D. S. Kirschen, "Situation awareness in power systems: Theory, challenges and applications," *Electric Power Syst. Res.*, vol. 122, pp. 140–151, 2015.

[28] M. R. Endsley, "Situation awareness misconceptions and misunderstandings," *J. Cogn. Eng. Decis. Mak.*, vol. 9, no. 1, pp. 4–32, 2015.

[29] G. Maas, M. Bial, and J. Fijalkowski, "Final report-system disturbance on 4 november 2006," Union Coordination Transmiss. Electricity Europe, Tech. Rep, 2007.

[30] M. Cui, J. Wang, J. Tan, A. R. Florita, and Y. Zhang, "A novel event detection method using PMU data with high precision," *IEEE Trans. Power Syst.*, vol. 34, no. 1, pp. 454–466, Jan. 2019.

[31] S. S. Negi, N. Kishor, K. Uhlen, and R. Negi, "Event detection and its signal characterization in PMU data stream," *IEEE Trans. Ind. Informat.*, vol. 13, no. 6, pp. 3108–3118, Dec. 2017.

[32] I. Jolliffe, "Principal component analysis," *Technometrics*, vol. 45, no. 3, pp. 276–276, 2003.

[33] M. Rafferty, X. Liu, D. M. Laverty, and S. McLoone, "Real-time multiple event detection and classification using moving window PCA," *IEEE Trans. Smart Grid*, vol. 7, no. 5, pp. 2537–2548, Sep. 2016.

[34] T. Xu and T. Overbye, "Real-time event detection and feature extraction using PMU measurement data," in *Proc. IEEE Int. Conf. Smart Grid Commun.*, 2015, pp. 265–270.

[35] Y. Zhou, R. Arghandeh, I. Konstantakopoulos, S. Abdullah, A. von Meier, and C. J. Spanos, "Abnormal event detection with high resolution micro-PMU data," in *Proc. Power Syst. Comput. Conf.*, 2016, pp. 1–7.

[36] M. Ibrahim and M. M. Salama, "Smart distribution system volt/VAR control using distributed intelligence and wireless communication," *IET Gener. Transmiss. Distrib.*, vol. 9, no. 4, pp. 307–318, 2015.

[37] A. N. M. M. Haque, T. H. Vo, and P. H. Nguyen, "Distributed intelligence: Unleashing flexibilities for congestion management in smart distribution networks (*invited paper*)," in *Proc. IEEE Int. Conf. Sustain. Energy Technol.*, 2016, pp. 407–413.

[38] C.-S. Karavas, G. Kyriakarakos, K. G. Arvanitis, and G. Papadakis, "A multi-agent decentralized energy management system based on distributed intelligence for the design and control of autonomous polygeneration microgrids," *Energy Convers. Manage.*, vol. 103, pp. 166–179, 2015.

[39] R. Piacentini, "Modernizing power grids with distributed intelligence and smart grid-ready instrumentation," in *Proc. IEEE PES Innov. Smart Grid Technol.*, 2012, pp. 1–6.

[40] S. Patil, G. Zhabelova, V. Vyatkin, and B. McMillin, "Towards formal verification of smart grid distributed intelligence: FREEDM case," in *Proc. IECON - 41st Annu. Conf. IEEE Ind. Electron. Soc.*, 2015, pp. 003974–003979.

[41] S. Wang, L. Li, and P. Dehghanian, "Distributed intelligence for online situational awareness in power grids," *Electron. Appendix*, pp. 1–4, Accessed: Nov. 2021. [Online]. Available: https://blogs.gwu.edu/seas-payman-lab/files/2019/02/smuApp-1.pdf

[42] C. Torrence and G. P. Compo, "A practical guide to wavelet analysis," *Amer. Meteorological Soc.*, vol. 79, no. 1, pp. 61–78, 1998.

[43] P. S. Addison, *The Illustrated Wavelet Transform Handbook: Introductory Theory and Applications in Science, Engineering, Medicine and Finance*. Boca Raton, FL, USA: CRC Press, 2017, pp. 15–23.
[44] A. Krizhevsky, I. Sutskever, and G. E. Hinton, "Imagenet classification with deep convolutional neural networks," in *Proc. Adv. Neural Inf. Process. Syst.*, 2012, pp. 1097–1105.
[45] K. Simonyan and A. Zisserman, "Very deep convolutional networks for large-scale image recognition," 2015, *arXiv:1409.1556*.
[46] L. A. Gatys, A. S. Ecker, and M. Bethge, "Image style transfer using convolutional neural networks," in *Proc. IEEE Conf. Comput. Vis. Pattern Recognit.*, 2016, pp. 2414–2423.
[47] A. Karpathy, "Convolutional neural networks for visual recognition," 2019. Accessed: Feb., 2021. [Online]. Available: http://cs231n.github.io/optimization-1/
[48] Y. Bengio, A. Courville, and P. Vincent, "Representation learning: A review and new perspectives," *IEEE Trans. Pattern Anal. Mach. Intell.*, vol. 35, no. 8, pp. 1798–1828, Aug. 2013.
[49] I. Goodfellow, Y. Bengio, and A. Courville, *Deep Learning*. Cambridge, MA, USA: MIT Press, 2016, pp. 339–364. [Online]. Available: http://www.deeplearningbook.org
[50] J. Hubbard, "Calculation of partition functions," *Phys. Rev. Lett.*, vol. 3, no. 2, pp. 77–78, 1959.
[51] J. A. de la O Serna, "Dynamic phasor estimates for power system oscillations," *IEEE Trans. Instrum. Meas.*, vol. 56, no. 5, pp. 1648–1657, Oct. 2007.
[52] N. Srivastava, G. Hinton, A. Krizhevsky, I. Sutskever, and R. Salakhutdinov, "Dropout: A simple way to prevent neural networks from overfitting," *J. Mach. Learn. Res.*, vol. 15, no. 1, pp. 1929–1958, 2014.
[53] P. Castello, J. Liu, C. Muscas, P. A. Pegoraro, F. Ponci, and A. Monti, "A fast and accurate PMU algorithm for P M class measurement of synchrophasor and frequency," *IEEE Trans. Instrum. Meas.*, vol. 63, no. 12, pp. 2837–2845, Dec. 2014.

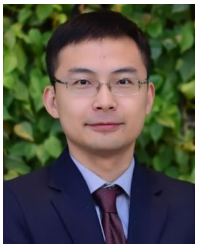

Shiyuan Wang (Member, IEEE) received the B.Eng. degree in mechanical engineering from the University of Science and Technology Beijing, Beijing, China, in 2012, and the M.Sc. and Ph.D. degrees in electrical engineering from The George Washington University, Washington, DC, USA, in 2014 and 2020, respectively. He is currently an Electric Power Engineer with Advanced Transmission Solution Team, Quanta Technology, LLC. His research interests include power system reliability and resiliency, smart grid and renewable energy, power grid harmonic analysis, and application of signal processing in power systems and energy analytics.

Li Li (Member, IEEE) received the B.Sc. degree in control engineering from Jilin University, Changchun, China, in 2008, and the M.Sc. and Ph.D. degrees in electrical engineering from The George Washington University, Washington, DC, USA, in 2014 and 2021, respectively. He is currently a Member of Technical Staff with the Machine Learning Software Engineering (MLSE) Team, Advanced Micro Devices (AMD). His research interests include image processing, artificial neural networks, and machine learning.

Payman Dehghanian (Senior Member, IEEE) received the B.Sc. degree in electrical engineering from the University of Tehran, Tehran, Iran, in 2009, the M.Sc. degree in electrical engineering from the Sharif University of Technology, Tehran, in 2011, and the Ph.D. degree in electrical engineering from Texas A&M University, College Station, TX, USA, in 2017. He is currently an Assistant Professor with the Department of Electrical and Computer Engineering, George Washington University, Washington, DC, USA. His research interests include power system reliability and resilience assessment, data-informed decision-making for asset management in electrical systems, and smart electricity grid applications.

Dr. Dehghanian was the recipient of the 2014 and 2015 IEEE Region five Outstanding Professional Achievement Awards, the 2015 IEEE-HKN Outstanding Young Professional Award, and the 2021 Early Career Award from the Washington Academy of Sciences.